

High index contrast photonic platforms for on-chip Raman spectroscopy

ALI RAZA,^{1,2,*}  STÉPHANE CLEMMEN,^{1,2,3}  PIETER WUYTENS,^{1,2}  MICHEL DE GOEDE,⁴ AMY S. K. TONG,⁵  NICOLAS LE THOMAS,^{1,2}  CHENGYU LIU,⁶ JIN SUNTIVICH,^{7,8} ANDRE G. SKIRTACH,^{2,9} SONIA M. GARCIA-BLANCO,⁴  DANIEL J. BLUMENTHAL,¹⁰  JAMES S. WILKINSON,⁵  AND ROEL BAETS^{1,2} 

¹Photonics Research Group, INTEC Department, Ghent University-imec, Technologiepark-Zwijnaarde, 9052 Ghent, Belgium

²Center for Nano- and Biophotonics, Ghent University, Belgium

³Laboratoire d'information quantique, Université Libre de Bruxelles, 1050 Bruxelles, Belgium

⁴Optical Sciences Group, MESA + Institute of Nanotechnology, University of Twente, 4617, The Netherlands

⁵Optoelectronics Research Centre (ORC), University of Southampton, Highfield, Southampton, SO17 1BJ, UK

⁶School of Applied and Engineering Physics, Cornell University, Ithaca, NY 14853, USA

⁷Materials Science and Engineering Department, Cornell University, Ithaca, NY 14853, USA

⁸Kavli Institute at Cornell for Nanoscale Science, Cornell University, Ithaca, NY 14853, USA

⁹Department of Biotechnology, Ghent University, Ghent, Belgium

¹⁰Optical Communications and Photonic Integration Group (OCPI), UC Santa Barbara (UCSB), Santa Barbara, CA 93106, USA

*ali.raza@ugent.be

Abstract: Nanophotonic waveguide enhanced Raman spectroscopy (NWERS) is a sensing technique that uses a highly confined waveguide mode to excite and collect the Raman scattered signal from molecules in close vicinity of the waveguide. The most important parameters defining the figure of merit of an NWERS sensor include its ability to collect the Raman signal from an analyte, i.e. “the Raman conversion efficiency” and the amount of “Raman background” generated from the guiding material. Here, we compare different photonic integrated circuit (PIC) platforms capable of on-chip Raman sensing in terms of the aforementioned parameters. Among the four photonic platforms under study, tantalum oxide and silicon nitride waveguides exhibit high signal collection efficiency and low Raman background. In contrast, the performance of titania and alumina waveguides suffers from a strong Raman background and a weak signal collection efficiency, respectively.

© 2019 Optical Society of America under the terms of the [OSA Open Access Publishing Agreement](https://doi.org/10.1364/OE.27.023067)

1. Introduction

High index contrast (HIC) waveguide structures allow a guided pump beam to interact efficiently with an analyte present in its vicinity. The analyte is excited using the waveguide mode and the scattered signal couples back to the same waveguide. This waveguide based excitation and collection technique can be used for different sensing phenomena, e.g. on-chip fluorescence [1], spontaneous Raman [2], stimulated Raman [3] and surface enhanced Raman spectroscopy [4], whereby unlike confocal approaches, the signal scales with the waveguide length. Different photonic structures i.e. optical fibers [5,6], planar waveguides [7], strip waveguides [8–12] and more recently slot waveguides [13] have been successfully used for this purpose. HIC waveguides of few millimeters length also provide the ease of use where an analyte can simply be drop casted unlike hollow core fibers [14]. An integrated photonic waveguide can, therefore, constitute the

sensing part of a Raman spectroscopic system and may provide enough signal enhancement to relax the usually stringent requirement on the optical source and detectors of a Raman system. HIC is very important in this context since the overall efficiency of the conversion of the guided pump to the guided Stokes beam depends critically on this contrast [2].

Ideally, the Raman sensor should enhance the scattered signal from the analyte without increasing any noise source. Obvious requirements of the photonic waveguide platform are, therefore: transparency in the visible-NIR wavelength range, photo-stability up to large intensities and a low level of fluorescence or Raman background from the waveguide material. Increasing the signal is largely achieved by increasing the interaction length. The limitation on this length is set primarily by absorption and imperfect fabrication of the waveguide. The second element at play for increasing the signal is by putting a large fraction of the field into the analyte rather than in the core material while maintaining proper guiding. This involves finding an optimized geometry that depends on the refractive index of the guiding material [2]. Previous reports showed that a major limitation of waveguide-enhanced Raman spectroscopy is the shot noise associated to background Raman scattering of the guiding material [15–17]. However, a systematic comparative study of the different materials typically used for waveguide-enhanced Raman spectroscopy has not been done before.

In this paper, Raman background of the four photonic platforms (Al_2O_3 , Si_3N_4 , Ta_2O_5 and TiO_2) is compared, both in terms of spectral features as well as absolute strength. Next, the signal collection efficiency of each photonic platform is characterized using ethanol as an analyte. Finally, a figure of merit for an optimized waveguide cross section of all the waveguide materials is established allowing a comparison of the four different platforms for their use as Raman sensor.

2. Methods

2.1. Investigated photonic platforms and fabrication details

Considering the high transparency in the near infrared wavelength region and ability to withstand large optical intensities, four photonic platforms i.e. Alumina (Al_2O_3), Silicon Nitride (Si_3N_4), Tantalum (Ta_2O_5) and Titania (TiO_2) are investigated. Besides the aforementioned material properties, these photonic platforms also hold the promise of integration of more functionalities such as spectral filtering of the pump beam [18,19], spectrometers [20,21], possibly lasers [22,23] and detectors [24], that can lead to a complete on-chip Raman spectroscopic system. Silicon shows a rather low background is not discussed here because its low bandgap make it incompatible with Raman instrumentation [25]. For the sake of simplicity and ease of fabrication, we have limited the waveguide design to a strip waveguide. However, it is worth mentioning that the gap structures e.g. sub-wavelength grating (SWG) and narrow slot waveguide offer many folds of signal enhancement as compared to a strip or rib waveguide [26].

Si_3N_4 strip waveguides used for our experiments are fabricated on a 200 mm silicon wafer containing a stack of $2.3 \pm 0.1 \mu\text{m}$ thick high-density plasma enhanced chemical vapor deposition (PECVD) silicon dioxide SiO_2 and 220 nm thick PECVD Si_3N_4 [27]. The structures were patterned with 193 nm optical lithography and subsequently etched by fluorine based inductive coupled plasma-reactive ion-etch process to attain the final structure. For alumina waveguides, a 450 nm thick Al_2O_3 layer was deposited on a thermally oxidized 100-mm Si wafer using an AJA ATC 1500 sputtering system. The UV exposed resist coated samples are inductively coupled plasma (ICP) etched using Oxford Plasma lab 100 (5:2, BCl_3 : HBr). TiO_2 bus waveguides are fabricated by a standard top-down procedure [11]. First, we deposit a 180 nm thick TiO_2 film on a thermal oxidized silicon wafer by reactive sputtering. Next, we apply a bilayer stack of anti-reflective coating and UV-210 photoresist on the wafer. Then, the patterns are defined by a deep-ultraviolet stepper ($\lambda = 248 \text{ nm}$) and transferred under C_4F_6 plasma etching with He cooling. Similarly, a 220 nm thick film of Ta_2O_5 was deposited onto oxidized silicon wafers using an OIPT Plasmalab 400 RF magnetron sputtering system [10] and annealed in oxygen

for 2 hours at 600C. Electron beam lithography (Jeol JBX 9300) followed by argon ion milling (OIPT Plasmafab 300 Plus) was used to produce rib waveguides of widths ranging from 500 nm to 700 nm. The geometry and optical properties of the fabricated waveguides are summarized in Table 1. The waveguide length (L) of Si_3N_4 and Ta_2O_5 is 1 cm each. While the waveguide lengths of Al_2O_3 and TiO_2 are 0.9 cm and 0.6 cm respectively.

Table 1. The optical properties of the photonic platforms. The η_A (analyte Raman signal conversion efficiency) and η_{BG} (waveguide Raman background conversion efficiency) are computed for 785 nm pump and 843 nm Stokes wavelength.

material	refractive index (n_c)	waveguide geometry (w×h) nm ²	loss, α_m (dB/cm)	η_A	η_{BG}
Al_2O_3	1.60	900 × 450	1.9–2.6	0.013	0.27
Si_3N_4	1.89	700 × 220	2.0–3.1	0.053	0.49
Ta_2O_5	2.11	500 × 220	4.8–5.4	0.13	0.61
TiO_2	2.33	380 × 180	7.0–8.0	0.18	0.79

2.2. Numerical modeling

The schematic of a HIC waveguide patterned on a thick silica (SiO_2) cladding is depicted in Fig. 1. The total backwards-propagating Stokes Raman signal $P_{sb}(\lambda_s)$ collected from an analyte of refractive index n_a using a strip waveguide of length L , width w and height h , can be estimated numerically using

$$\frac{P_{sb}(\lambda_s)}{P(\lambda_p)} = \frac{1}{2} \times \eta(w, h, \lambda_p, \lambda_s) \times \sigma \times \rho \times \overbrace{\left(\frac{1 - e^{-2\alpha L}}{2\alpha} \right)}^{\text{Length factor}} \quad (1)$$

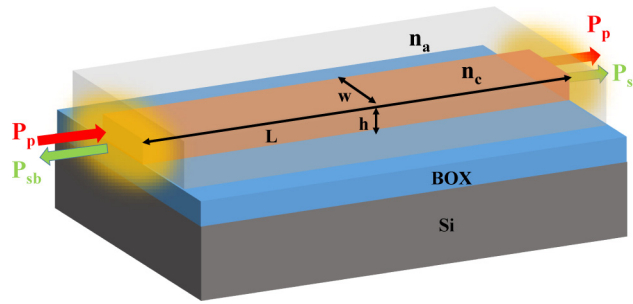


Fig. 1. The schematic of a patterned HIC waveguide. n_c and n_a are the refractive index of core and analyte (top cladding) respectively.

where η is the Raman conversion efficiency that depends on the modal properties of the waveguide. Details of η is given in the Appendix A.1. ρ and σ are the molecular density and differential Raman cross section of the analyte. The length factor represents the Raman signal dependence on the waveguide loss (α) and length (L). The Raman signal generated from the analyte and guiding material, propagates evenly in forward as well as backward direction. However, due to the different waveguide loss conditions faced by both signals, their dependence on the waveguide length is also different. The length factor (LF) mentioned in Eq. (1) slowly saturates. In contrast to that case, there exists an optimal length when collecting the forward generated Raman signal because the Raman signal has to travel through the whole length of the waveguide [2]. This is illustrated in Fig. 2, which shows the length factor for both collection

strategies assuming $\alpha = \alpha_p = \alpha_s = 5$ dB/cm. For the sake of clarity and because it may be desirable to collect the Raman signal in the forward direction, we introduce the saturation length $L_s = 1/\alpha$ in Fig. 2. For a waveguide length greater than L_s , the forward propagating signal decays due to the subsequent waveguide losses. Also, Fig. 2(b) illustrates that the LF decreases exponentially when the loss increases. The dotted lines represent the waveguide losses of the fabricated Al_2O_3 , Si_3N_4 , Ta_2O_5 and TiO_2 waveguides. The COMSOL finite element mode solver is used to calculate η . The fundamental TE mode is excited and ethanol is used as an analyte ($n_A = 1.37$). The simulations are performed assuming a 785 nm pump wavelength and 843 nm Stokes wavelength. This corresponds to the 880 cm^{-1} Raman mode of ethanol due to the symmetric C–C–O stretch [28]. The values of η_A and η_{BG} for the four waveguides are reported in Table 1. The waveguide cross section ($w \times h$) for each material is selected in such a way that it supports only one TE mode in the wavelength span of 780 – 900 nm. No waveguide geometry is ideal because of the technological limitations in fabricating the ideal waveguide. However, we will discuss the ideal strip geometries hereafter. The waveguide loss reported in Table 1 is measured at 800 nm wavelength for water cladded waveguides.

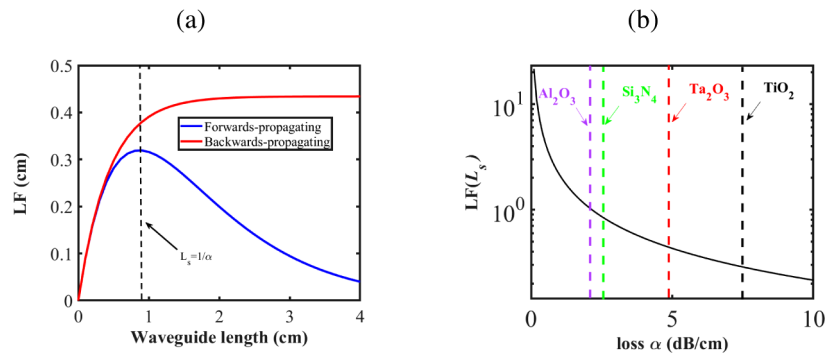


Fig. 2. a) The length factor (LF) comparison for a forward (blue) and a backward (red) propagating Raman signal assuming a fixed waveguide loss of $\alpha = 5$ dB/cm. b) The length factor (LF) increases for decreasing loss. The dotted lines show the value of the LF at their saturation length L_s for the four different types of waveguides.

2.3. Measurement setup

The Raman measurements are performed using a confocal Raman microscope (WITEC Alpha300R+). The schematic of the optical setup is shown in Fig. 3. The photonic chip is positioned vertically under the high NA objective (0.63 NA, 40 \times) i.e., light is coupled in and the Raman signal is collected out of the chip from the same cleaved facet. A Toptica XTRA II diode laser pumping at 785 nm wavelength is used and the polarization is set to excite the TE mode of the waveguide. A laser power of 10 mW is measured before the objective. The scattered signal collected in back reflection is imaged on a 100 μm multimode fiber. This fiber functions as confocal pinhole and entrance slit for guiding the Stokes scattered light into the spectrometer, which uses a 600 lines/mm grating to disperse the light onto a $-70\text{ }^\circ\text{C}$ cooled CCD camera (ANDOR iDus 401 BR–DD). The objective and chip were aligned with a 100 nm precision based on the maximum intensity of the waveguide's Raman spectrum. Simultaneously, maximum light scattering along the waveguide was observed from a camera imaging the top-surface of the chip. All spectra were acquired with 0.25 sec integration time. At least five waveguides per chip were measured.

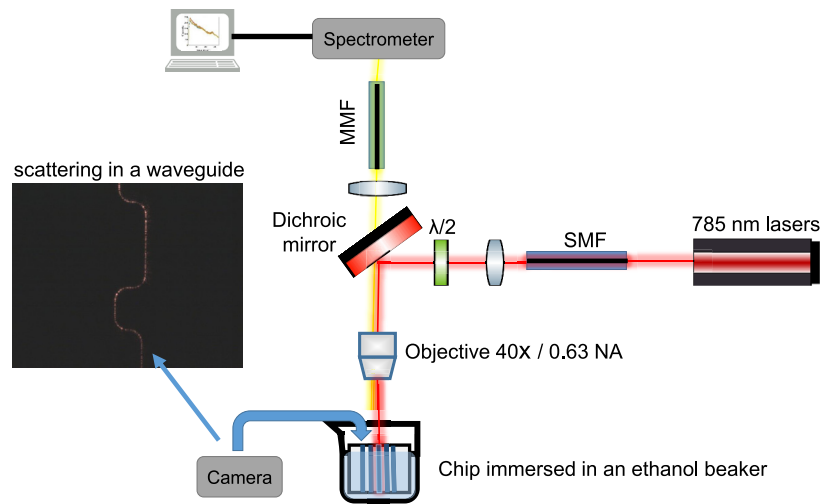


Fig. 3. The schematic of an optical setup used for Raman measurements. The left inset shows the light scattering of a waveguide imaged by the side camera. SMF = single mode fiber and MMF = multi-mode fiber.

3. Results and discussion

First of all, each chip is measured without ethanol to obtain insight in its intrinsic background scattering. All four waveguides have different lengths so that a fair comparison requires to normalize those spectra by their optimal length $LF(L_s)$ and by the coupling efficiency. The coupling efficiencies measured using high NA objective (0.63 NA, 40 \times) to Al_2O_3 , Si_3N_4 , Ta_2O_5 and TiO_2 waveguides are ≈ 2.9 , 3.7, 8.3 and 7.9 dB/facet. The measured normalized Stokes spectra are shown in Fig. 4. The shaded areas represent the standard deviation of 5 different spectra for each waveguide material. This standard deviation is attributed to different coupling efficiencies and waveguide losses of the waveguides on the same chip. The TiO_2 scattering spectrum is scaled down by 1/8 to plot all the spectra in one window. From these measurements, it can be seen that the TiO_2 has by far the strongest background scattering. In order to validate this huge background, another TiO_2 chip is also fabricated with the different process parameters (See Appendix A.2). Both TiO_2 chips exhibit very similar Raman background both in the terms of the spectral features as well as the Raman background strength. PECVD Si_3N_4 and Ta_2O_5 exhibit comparable Raman background, that is approximately 8 times weaker than TiO_2 . Also, PECVD Si_3N_4 , Ta_2O_5 and TiO_2 shows relatively high Raman background in the 0–700 cm^{-1} range and then much lower background at high Raman shifts. In the Ta_2O_5 Raman background, a major characteristic Raman band at 660 cm^{-1} corresponds to the Ta–O stretching vibrations of TaO_6 octahedra [29]. Al_2O_3 shows the weakest Raman background that mostly stays flat along the span of 50 – 1800 cm^{-1} Raman shift. This characterization also shows that the background strength increases with the refractive index.

In order to discern the fluorescent contribution, each waveguide background is also measured at 633 nm pump wavelength. Due to different modal properties of the waveguide at 633 and 785 nm wavelength, each spectrum is normalized by its maximum counts. The results are shown in Fig. 5. Al_2O_3 exhibits slightly different background at higher wavenumbers ($>1000 \text{ cm}^{-1}$)[30]. No significant change is observed in the spectral features of the Raman background of the other three materials. This confirms no or minimal contribution of auto-fluorescence to the recorded Raman background.

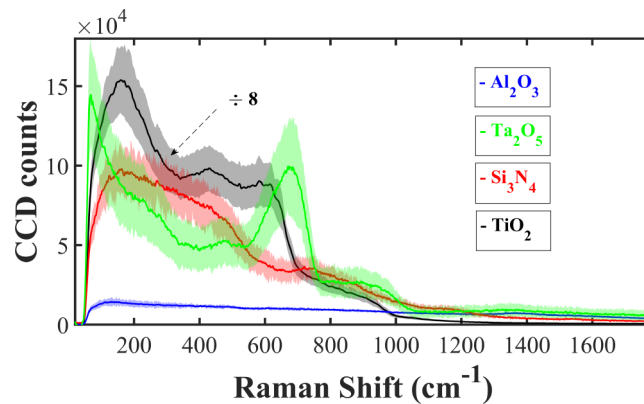


Fig. 4. The Raman background measured from air clad waveguides of Al_2O_3 , Si_3N_4 , Ta_2O_5 and TiO_2 . All spectra are scaled to its respective optimized length $LF(L_s)$.

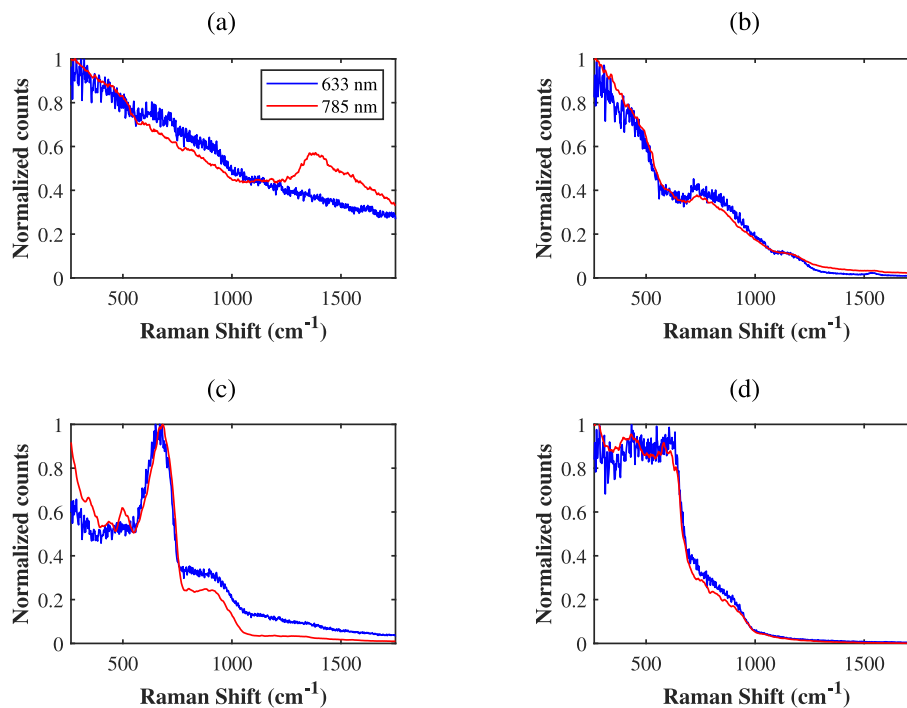


Fig. 5. The Raman spectrum of a) Al_2O_3 , b) Si_3N_4 , c) Ta_2O_5 and TiO_2 measured using 633 nm (blue) and 785 nm (red) pump wavelength.

In a second set of measurements, the Al_2O_3 , Si_3N_4 , Ta_2O_5 and TiO_2 chips are immersed into a beaker containing ethanol. Each chip is immersed in such a way that few micrometers length of the waveguide is in the air. Each spectrum is recorded after optimizing the strength of the 880 cm^{-1} Raman mode of ethanol. The spectra are shown in Fig. 6(a). Each spectrum is normalized by the coupling efficiency and rescaled to its optimal length factor $LF(L_s)$. On top of the strong broad band Raman background of the guiding material, the Raman modes of ethanol are clearly present. The dotted lines represent the 880 , 1054 , 1098 , 1275 and 1456 cm^{-1} Raman vibrations of ethanol. To characterize the relative signal strength, the signal (C_{sig}) and the background

(C_{BG}) counts at 880 cm^{-1} are extracted as shown in Fig. 6(b) (inset). As depicted in Fig. 6(b), for the 880 cm^{-1} Raman shift, $C_{sig,SiN} / C_{sig,AlO} \approx 3.63 \pm 0.45$, $C_{sig,TaO} / C_{sig,AlO} \approx 4.84 \pm 0.81$ and $C_{sig,TiO} / C_{sig,AlO} \approx 6.01 \pm 1.6$. This is in good correspondence to what was predicted in Table 1. For example, if $\zeta_x = \eta_x \times LF(L_s)_x$ then $\zeta_{SiN} / \zeta_{AlO} = 3.44$, $\zeta_{TaO} / \zeta_{AlO} = 4.15$ and $\zeta_{TiO} / \zeta_{AlO} = 5.6$. It is worth mentioning that the higher index contrast of TiO_2 boosts the Raman signal strength i.e. $\eta_{TiO} \approx 14 \times \eta_{AlO}$. However, the higher waveguide losses, i.e. $\alpha_{TiO} = 7\text{--}8\text{ dB/cm}$, negate this overall enhancement.

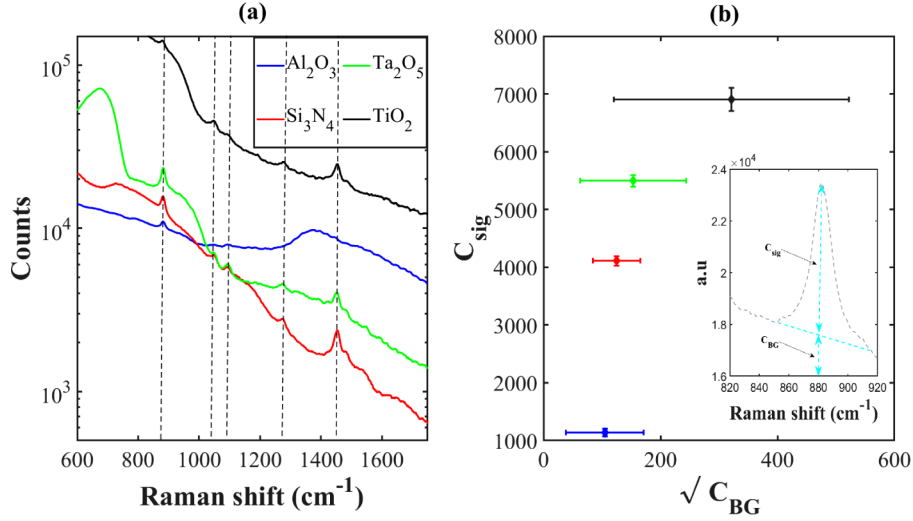


Fig. 6. a) The Raman spectra measured from an ethanol clad waveguides of Al_2O_3 , Si_3N_4 , Ta_2O_5 and TiO_2 . The dotted lines represent the 880, 1054, 1098, 1275 and 1456 cm^{-1} Raman modes of ethanol. b) The signal strength C_{sig} and background noise $\sqrt{C_{BG}}$ measured for 880 cm^{-1} Raman mode of ethanol. The inset shows the C_{sig} and C_{BG} .

Knowing the Raman background scattering and the capability of each photonic platform to collect a Raman signal from an analyte for a given waveguide geometry, we can now establish a figure of merit for an optimized waveguide cross section of each material. Thus far, we have used the measured waveguide losses α_m in our comparison. However, because technological progress are likely to change those loss values, we are now considering the case of identical waveguide loss across the four types of waveguides: we set $\alpha = 1\text{ dB/cm}$. The figure of merit (FOM) for an optimized waveguide geometry is defined as the ratio of analyte signal strength (C_{sig}^O) to Raman background shot noise ($\sqrt{C_{BG}^O}$) where

$$C_{sig}^O = C_{sig} \times \frac{\eta_{OA}}{\eta_A} \times \frac{(LF(L_s))_{\alpha=1dB/cm}}{(LF(L_s))_{\alpha=\alpha_m}} \quad (2)$$

and

$$C_{BG}^O = C_{BG} \times \frac{\eta_{OBG}}{\eta_{BG}} \times \frac{(LF(L_s))_{\alpha=1dB/cm}}{(LF(L_s))_{\alpha=\alpha_m}} \quad (3)$$

COMSOL based simulations are performed to optimize the waveguide cross section ($w_o \times h_o$). Again, we use ethanol as an analyte at the Raman detuning of the 880 cm^{-1} line. The range of width and height is chosen in such a way that the waveguide supports only one fundamental TE mode in the wavelength span 785 – 900 nm. The results are shown in Fig. 7. Clearly, the signal strength is stronger for high aspect ratio waveguide cross sections as expected for TE excitation.

This is due to the higher modal overlap with the analyte. Also, η_A for an optimized geometry improves with increasing refractive index of the core material. It is estimated that the Raman signal strength varies by nearly an order of magnitude between the optimal geometry of an Al_2O_3 waveguide ($\eta_A = 0.039$) and an optimal TiO_2 waveguide ($\eta_A = 0.375$). Also, owing to the stronger optical confinement, the optimal waveguide cross section scales to smaller dimensions for increasing index contrast e.g. $w_O \times h_O$ of Al_2O_3 and TiO_2 are $525 \text{ nm} \times 1125 \text{ nm}$ and $250 \text{ nm} \times 350 \text{ nm}$ respectively. The FOM for each waveguide is presented in Table 2. TiO_2 exhibits a large C_{sig}^O but the FOM is poor due to a large C_{BG}^O . Similarly for Al_2O_3 , the FOM suffers due to the low C_{sig}^O . On the other hand, due to the low Raman background and high Raman conversion efficiency, Si_3N_4 and Ta_2O_5 have a more or less equal FOM, which is 2.7 and 3.9 times higher as compared to Al_2O_3 and TiO_2 respectively.

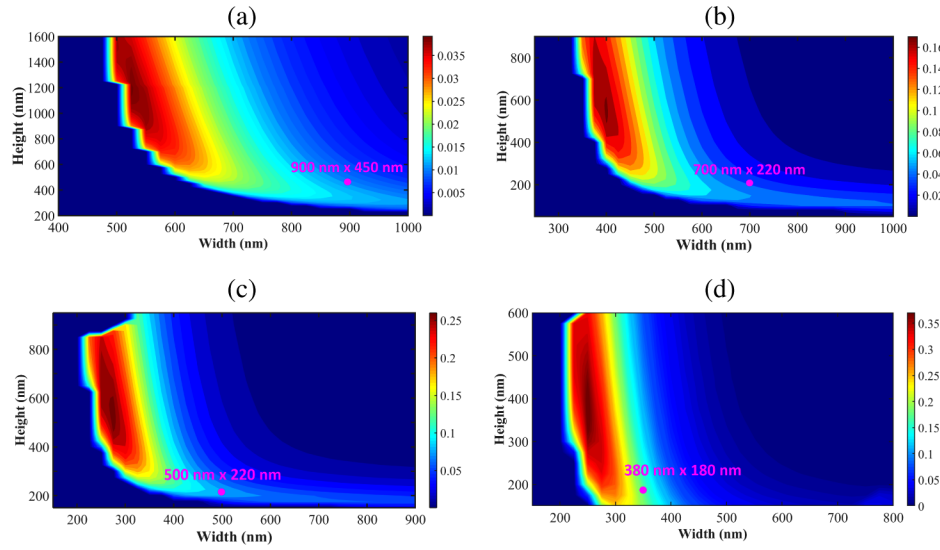


Fig. 7. The Raman conversion efficiency η_A at 880 cm^{-1} Stokes shift calculated for a) Al_2O_3 ($n=1.6$), b) Si_3N_4 ($n=1.9$), c) Ta_2O_5 ($n=2.11$) and TiO_2 ($n=2.36$). The scale of the color bar is same for comparison. The circle with magenta face color represents the dimensions of the fabricated waveguides.

Table 2. The estimated signal strength C_{sig}^O and Raman background C_{BG}^O for an optimized waveguide cross section $w_O \times h_O$. The optimal analyte Raman conversion efficiency (η_{OA}) is extracted from Fig. 7.

material	Al_2O_3	Si_3N_4	Ta_2O_5	TiO_2
$w_O \times h_O \text{ (nm}^2\text{)}$	525×1125	425×575	275×500	250×350
$\eta_{OA}(\text{optimal})$	0.039	0.172	0.266	0.375
C_{sig}^O (counts)	$\approx 0.7 \times 10^4$	$\approx 3.2 \times 10^4$	$\approx 4.9 \times 10^4$	$\approx 7.7 \times 10^4$
C_{BG}^O (counts)	$\approx 0.8 \times 10^4$	$\approx 1.1 \times 10^4$	$\approx 2.5 \times 10^4$	$\approx 1.4 \times 10^5$
$\text{FOM} = \frac{C_{sig}^O}{\sqrt{C_{BG}^O}}$	≈ 79	≈ 305	≈ 310	≈ 116

4. Conclusion

To conclude, we present here the performance of four different photonic integration platforms (Al_2O_3 , Si_3N_4 , Ta_2O_5 and TiO_2) as an on-chip Raman spectroscopy platform. The performance is compared in terms of the signal collection efficiency and the Raman background of the waveguide material. A first comparison is made accounting for the current technological fabrication capability and resulting propagation loss. A more general comparison is made that factors out the loss therefore looking forward at technological improvements. From this we can draw a number of conclusions. Due to the higher index contrast, TiO_2 waveguides exhibit the highest Raman conversion efficiency. However, the signal-to-background ratio is relatively poor due to the high Raman background. On the other hand, Al_2O_3 waveguides exhibit weak Raman background, but the signal collection efficiency suffers due to the low index contrast. Si_3N_4 and Ta_2O_5 strip waveguides seem to be nearly equally good platforms for Raman spectroscopy as their Raman background is rather low but their capability to collect the Raman signal from the analyte is strong. In practice, the loss in Si_3N_4 waveguides being lower than in Ta_2O_5 waveguides, it is presently more advantageous to use Si_3N_4 . With the progress in making low loss waveguides, any of the investigated photonic platform could become the best one as long as the waveguide loss is primarily due to the waveguide itself. In case the loss is dominated by the analyte, the figure of merit given in Table 2 gives a definite answer on what technology is ideal. The results presented in this paper will help to further improve the sensitivity of NWERS sensors. Along with other integrated photonics functionalities, these on-chip Raman sensors can be employed in many interesting application such as the detection of VOCs [31] in ambient air or sensing of bio-analytes in physiological concentration [32,33].

Appendix

A.1: Derivation of P_s/P_o

Assume a dipole is radiating at a frequency c/λ_s in a lossless surrounding medium of refractive index $n=\sqrt{\epsilon}$, at position \mathbf{r}_o in a close vicinity of a waveguide of width w and height h . For a weak coupling regime [34], the fraction of the total scattered power P_{wg} that couples to a waveguide mode ($\mathbf{E}(\mathbf{r}, \lambda_s)$, $\mathbf{H}(\mathbf{r}, \lambda_s)$) can be written as [35,36]

$$\frac{P_{wg}}{P_i} = \frac{3}{4\pi} \frac{c\lambda_s^2}{nv_g} \frac{1}{\mathbf{A}_{\text{eff}}} \quad (4)$$

where P_i , v_g and \mathbf{A}_{eff} are the total emitted power by a dipole in free space, group velocity and effective modal area respectively. A_{eff} of a given mode propagating in a non-dispersive media is defined as

$$\mathbf{A}_{\text{eff}} = \frac{1}{2} \frac{\iint \epsilon_o \epsilon |\mathbf{E}(\mathbf{r}, \lambda_s)|^2 + \mu_o |\mathbf{H}(\mathbf{r}, \lambda_s)|^2 d\mathbf{r}}{\epsilon_o \epsilon |\mathbf{E}(\mathbf{r}_o, \lambda_s)|^2} \quad (5)$$

The dipole strength $d(\mathbf{r}, \lambda_s)$ of a dipole excited by a waveguide mode $\mathbf{E}(\mathbf{r}, \lambda_p)$ of total guided power P_o can be written as [2,37]

$$|d(\mathbf{r}, \lambda_s)|^2 = \alpha^2 n_g P_o \frac{\epsilon |\mathbf{E}(\mathbf{r}_o, \lambda_p)|^2}{\iint \epsilon |\mathbf{E}(\mathbf{r}, \lambda_p)|^2 d\mathbf{r}} \quad (6)$$

where α and n_g are the molecular polarizability and group index of the guided mode. Using Eqs. (4), (5) and (6) and Raman cross section $\sigma = \frac{\pi^2 \alpha^2}{\epsilon_o^2 \lambda^4}$, the total power $P_{sb}(\lambda_s)$ coupling into

a waveguide mode in backward direction from the dipoles lying uniformly over a waveguide length of L_o with density ρ can be written as

$$\frac{P_{sb}(\lambda_s)}{P(\lambda_p)} = \frac{1}{2} \times \rho \times \sigma \times \eta_A(w, h, \lambda_p, \lambda_s) \int_0^{L_o} e^{-\alpha_s L} e^{-\alpha_p L} dL \quad (7)$$

where

$$\eta(w, h, \lambda_p, \lambda_s) = \frac{n_g^2 \lambda_s^2}{n} \iint \frac{\epsilon |\mathbf{E}(\mathbf{r}_o, \lambda_p)|^2}{\epsilon |\mathbf{E}(\mathbf{r}, \lambda_p)|^2} \frac{1}{\mathbf{A}_{\text{eff}}(\mathbf{r}_o, \lambda_s)} d\mathbf{r}_o \quad (8)$$

and α_p and α_s are the waveguide losses at pump and Stokes wavelength.

In Eq. (8), the outer integral runs over the area of interest. For example, to estimate the signal strength from an analyte lying over a waveguide, the integral runs over the top cladding i.e. $\eta = \eta_A$. Likewise, to estimate the waveguide background strength, the integral runs over the waveguide core i.e. $\eta = \eta_{BG}$. In Eq. (1), for the sake of simplicity, we assume same waveguide loss at pump and Stokes wavelength i.e. $\alpha = \alpha_p = \alpha_s$.

A.2: The Raman background comparison of two differently processed Titania waveguides

To validate the huge Raman background generated from the Titania waveguides, Raman background from two differently processed TiO_2 chips are measured and compared. The second TiO_2 chip (Sample 2) is fabricated with the different process parameters. A 100 nm thick TiO_2 layer is deposited using RF sputtering with the following parameters: 20 °C temperature, 6×10^{-3} mbar process pressure, 34 sccm Ar flow, 7.5 sccm O_2 flow and 500 W source power. After an e-beam exposure and resist development, the TiO_2 is etched using the reactive ion etching in an Oxford PlasmaPro 100 Cobra. The final waveguide has a cross section (w × height) of $1000 \times 100 \text{ nm}^2$. Figure 8(a) shows η_{BG} for Sample 1 (same sample as used in Fig. 4) and Sample 2 in the Raman shift span of 0–1600 cm^{-1} . The Raman background of Sample 2 is measured and compared with Sample 1. Due to the different waveguide cross section, both spectra are normalized by their respective $LF(L_s)$ and η_{BG} . As shown in Fig. 8(b), for the same input pump power, both spectra are remarkably aligned well with each other in terms of the spectral features. This result shows that two differently processed TiO_2 chips lead to the same Raman background. Note that the processing temperature in both TiO_2 chips is kept less than TiO_2 crystallization

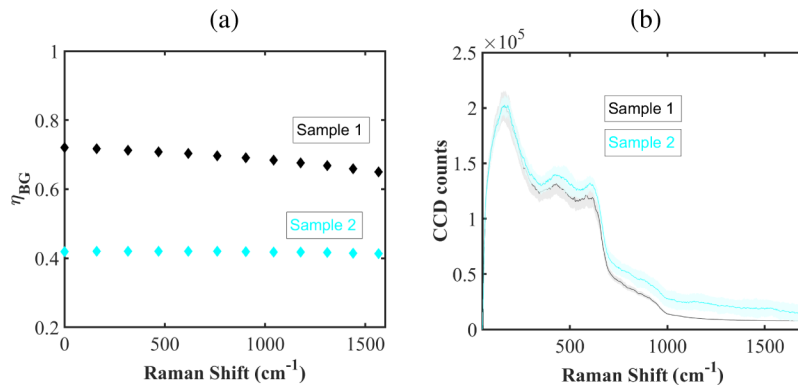


Fig. 8. a) The η_{BG} calculated using Eq. (8) and b) the Raman background comparison of two differently processed TiO_2 waveguides. Sample 1 is the same TiO_2 chip as used in Fig. 4. The waveguide cross sections of Sample 1 and Sample 2 are $180 \times 380 \text{ nm}^2$ and $100 \times 1000 \text{ nm}^2$ respectively.

temperature. A high-temperature growth of TiO_2 layers leads to the crystallization [38] that eventually changes the Raman background.

Funding

Fonds Wetenschappelijk Onderzoek (FWO); F.R.S–FNRS; Bijzonder Onderzoeksfonds (BOF); NSFMRSEC program (DMR-1719875); National Science Foundation (NSF) (NNCI-1542081); H2020 European Research Council (ERC).

Acknowledgments

The authors acknowledge Prof Pol Van Dorpe (imec) for useful discussion. The authors also thank Dr. Chang Chen for the measurements at imec. We acknowledge support from the Samsung Advanced Institute of Technology (SAIT) through the Global Research Outreach (GRO). This work was also partially supported by the Cornell Center for Materials Research and the Cornell NanoScale Facility, a member of the National Nanotechnology Coordinated Infrastructure (NNCI).

References

1. M. Mahmud-Ul-Hasan, P. Neutens, R. Vos, L. Lagae, and P. Van Dorpe, "Suppression of bulk fluorescence noise by combining waveguide-based near-field excitation and collection," *ACS Photonics* **4**(3), 495–500 (2017).
2. A. Dhakal, A. Raza, F. Peyskens, A. Z. Subramanian, S. Clemmen, N. Le Thomas, and R. Baets, "Efficiency of evanescent excitation and collection of spontaneous Raman scattering near high index contrast channel waveguides," *Opt. Express* **23**(21), 27391–27404 (2015).
3. H. Zhao, S. Clemmen, A. Raza, and R. Baets, "Stimulated Raman spectroscopy of analytes evanescently probed by a silicon nitride photonic integrated waveguide," *Opt. Lett.* **43**(6), 1403–1406 (2018).
4. A. Raza, S. Clemmen, P. Wuytens, M. Muneeb, M. Van Daele, J. Dendooven, C. Detavernier, A. Skirtach, and R. Baets, "ALD assisted nanoplasmonic slot waveguide for on-chip enhanced Raman spectroscopy," *APL Photonics* **3**(11), 116105 (2018).
5. F. Benabid, J. C. Knight, G. Antonopoulos, and P. S. J. Russell, "Stimulated Raman scattering in hydrogen-filled hollow-core photonic crystal fiber," *Science* **298**(5592), 399–402 (2002).
6. S. O. Konorov, C. J. Addison, H. G. Schulze, R. F. B. Turner, and M. W. Blades, "Hollow-core photonic crystal fiber-optic probes for Raman spectroscopy," *Opt. Lett.* **31**(12), 1911–1913 (2006).
7. J. S. Kanger, C. Otto, M. Slotboom, and J. Greve, "Waveguide Raman spectroscopy of thin polymer layers and monolayers of biomolecules using high refractive index waveguides," *J. Phys. Chem.* **100**(8), 3288–3292 (1996).
8. A. Pope, A. Schulte, Y. Guo, L. Ono, B. R. Cuenya, C. Lopez, K. Richardson, K. Kitanovski, and T. Wittingham, "Chalcogenide waveguide structures as substrates and guiding layers for evanescent wave Raman spectroscopy of bacteriorhodopsin," *Vib. Spectrosc.* **42**(2), 249–253 (2006).
9. A. Dhakal, A. Z. Subramanian, P. Wuytens, F. Peyskens, N. Le Thomas, and R. Baets, "Evanescent excitation and collection of spontaneous Raman spectra using silicon nitride nanophotonic waveguides," *Opt. Lett.* **39**(13), 4025–4028 (2014).
10. Z. Wang, M. N. Zervas, P. N. Bartlett, and J. S. Wilkinson, "Surface and waveguide collection of Raman emission in waveguide-enhanced Raman spectroscopy," *Opt. Lett.* **41**(17), 4146–4149 (2016).
11. C. C. Evans, C. Liu, and J. Suntivich, "TiO₂ nanophotonic sensors for efficient integrated evanescent Raman spectroscopy," *ACS Photonics* **3**(9), 1662–1669 (2016).
12. S. A. Holmstrom, T. H. Stievater, D. A. Kozak, M. W. Pruessner, N. Tyndall, W. S. Rabinovich, R. A. McGill, and J. B. Khurgin, "Trace gas Raman spectroscopy using functionalized waveguides," *Optica* **3**(8), 891–896 (2016).
13. A. Dhakal, P. C. Wuytens, F. Peyskens, K. Jans, N. Le Thomas, and R. Baets, "Nanophotonic waveguide enhanced Raman spectroscopy of biological submonolayers," *ACS Photonics* **3**(11), 2141–2149 (2016).
14. P. S. Donvalkar, S. Ramelow, S. Clemmen, and A. L. Gaeta, "Continuous generation of rubidium vapor in hollow-core photonic bandgap fibers," *Opt. Lett.* **40**(22), 5379–5382 (2015).
15. J. May and Y.-S. Li, "Fiber Raman background study and its application in setting up optical fiber Raman probes," *Appl. Opt.* **35**(15), 2527–2533 (1996).
16. A. Dhakal, P. Wuytens, A. Raza, N. Le Thomas, and R. Baets, "Silicon nitride background in nanophotonic waveguide enhanced Raman spectroscopy," *Materials* **10**(2), 140 (2017).
17. N. Le Thomas, A. Dhakal, A. Raza, F. Peyskens, and R. Baets, "Impact of fundamental thermodynamic fluctuations on light propagating in photonic waveguides made of amorphous materials," *Optica* **5**(4), 328–336 (2018).
18. A. Gondarenko, J. S. Levy, and M. Lipson, "High confinement micron-scale silicon nitride high Q ring resonator," *Opt. Express* **17**(14), 11366–11370 (2009).
19. X. Nie, N. Turk, Y. Li, Z. Liu, and R. Baets, "High extinction ratio on-chip pump-rejection filter based on cascaded grating-assisted contra-directional couplers in silicon nitride rib waveguides," *Opt. Lett.* **44**(9), 2310–2313 (2019).
20. X. Nie, E. Ryckboer, G. Roelkens, and R. Baets, "CMOS-compatible broadband co-propagative stationary fourier transform spectrometer integrated on a silicon nitride photonics platform," *Opt. Express* **25**(8), A409–A418 (2017).

21. D. Martens, A. Z. Subramanian, S. Pathak, M. Vanslembrouck, P. Bienstman, W. Bogaerts, and R. Baets, "Compact silicon nitride arrayed waveguide gratings for very near-infrared wavelengths," *IEEE Photonics Technol. Lett.* **27**(2), 137–140 (2015).
22. Z. Zhou, B. Yin, and J. Michel, "On-chip light sources for silicon photonics," *Light: Sci. Appl.* **4**(11), e358 (2015).
23. E. P. Haglund, S. Kumari, P. Westbergh, J. S. Gustavsson, G. Roelkens, R. Baets, and A. Larsson, "Silicon-integrated short-wavelength hybrid-cavity vcsel," *Opt. Express* **23**(26), 33634–33640 (2015).
24. J. Michel, J. Liu, and L. C. Kimerling, "High-performance ge-on-si photodetectors," *Nat. Photonics* **4**(8), 527–534 (2010).
25. S. Clemmen, A. Perret, J. Safioui, W. Bogaerts, R. Baets, S.-P. Gorza, P. Emplit, and S. Massar, "Low-power inelastic light scattering at small detunings in silicon wire waveguides at telecom wavelengths," *J. Opt. Soc. Am. B* **29**(8), 1977–1982 (2012).
26. D. M. Kita, J. Michon, S. G. Johnson, and J. Hu, "Are slot and sub-wavelength grating waveguides better than strip waveguides for sensing?" *Optica* **5**(9), 1046–1054 (2018).
27. A. Z. Subramanian, P. Neutens, A. Dhakal, R. Jansen, T. Claes, X. Rottenberg, F. Peyskens, S. Selvaraja, P. Helin, B. Du Bois, K. Leyssens, S. Severi, P. Deshpande, R. Baets, and P. Van Dorpe, "Low-loss singlemode PECVD Silicon Nitride photonic wire waveguides for 532–900 nm wavelength window fabricated within a cmos pilot line," *IEEE Photonics J.* **5**(6), 2202809 (2013).
28. A. Nordon, A. Mills, R. T. Burn, F. M. Cusick, and D. Littlejohn, "Comparison of non-invasive NIR and Raman spectrometries for determination of alcohol content of spirits," *Anal. Chim. Acta* **548**(1-2), 148–158 (2005).
29. T. Tsuchiya, H. Imai, S. Miyoshi, P.-A. Glans, J. Guo, and S. Yamaguchi, "X-ray absorption, photoemission spectroscopy, and Raman scattering analysis of amorphous tantalum oxide with a large extent of oxygen nonstoichiometry," *Phys. Chem. Chem. Phys.* **13**(38), 17013–17018 (2011).
30. A. Mortensen, D. Christensen, O. F. Nielsen, and E. Pedersen, "Broad background bands in Raman spectra of alumina studied by both visible and near-infrared excitation," *J. Raman Spectrosc.* **24**(10), 667–673 (1993).
31. C. L. Wong, U. Dinish, M. S. Schmidt, and M. Olivo, "Non-labeling multiplex surface enhanced Raman scattering (sers) detection of volatile organic compounds (voecs)," *Anal. Chim. Acta* **844**, 54–60 (2014).
32. P. -H. Hsu and H. K. Chiang, "Surface-enhanced Raman spectroscopy for quantitative measurement of lactic acid at physiological concentration in human serum," *J. Raman Spectrosc.* **41**(12), 1610–1614 (2010).
33. H. Cho, S. Kumar, D. Yang, S. Vaidyanathan, K. Woo, I. Garcia, H. J. Shue, Y. Yoon, K. Ferreri, and H. Choo, "Surface-enhanced Raman spectroscopy-based label-free insulin detection at physiological concentrations for analysis of islet performance," *ACS Sens.* **3**(1), 65–71 (2018). PMID: 29322773.
34. T. Hümmer, F. García-Vidal, L. Martín-Moreno, and D. Zueco, "Weak and strong coupling regimes in plasmonic QED," *Phys. Rev. B* **87**(11), 115419 (2013).
35. Y. C. Jun, R. D. Kekatpure, J. S. White, and M. L. Brongersma, "Nonresonant enhancement of spontaneous emission in metal-dielectric-metal plasmon waveguide structures," *Phys. Rev. B* **78**(15), 153111 (2008).
36. Y. C. Jun, R. M. Briggs, H. A. Atwater, and M. L. Brongersma, "Broadband enhancement of light emission in silicon slot waveguides," *Opt. Express* **17**(9), 7479–7490 (2009).
37. F. Peyskens, A. Dhakal, P. Van Dorpe, N. Le Thomas, and R. Baets, "Surface enhanced Raman spectroscopy using a single mode nanophotonic-plasmonic platform," *ACS Photonics* **3**(1), 102–108 (2016).
38. Q. Xie, J. Musschoot, D. Deduytsche, R. L. Van Meirhaeghe, C. Detavernier, S. Van den Berghe, Y.-L. Jiang, G.-P. Ru, B.-Z. Li, and X.-P. Qu, "Growth kinetics and crystallization behavior of TiO₂ films prepared by plasma enhanced atomic layer deposition," *J. Electrochem. Soc.* **155**(9), H688–H692 (2008).